Particle Physics at CERN

Annual Report 2004

Y. Allkofer, C. Amsler, V. Chiochia, A. Dorokhov, C. Hörmann,
I. Johnson, K. Prokofiev, H. Pruys, C. Regenfus, P. Robmann,
J. Rochet, T. Speer, S. Steiner, and D. Tsirigkas

Secretariat: P. Perréard

Physik-Institut der Universität Zürich
Winterthurerstrasse 190, CH-8057 Zürich, Switzerland

April 5, 2005

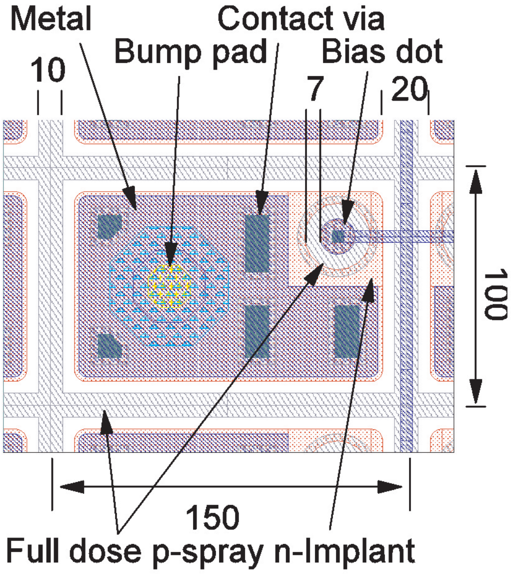

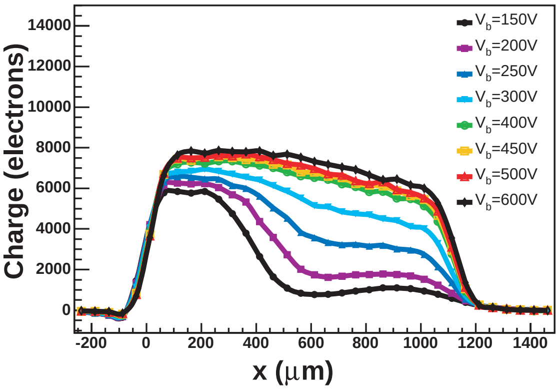

Contents

This report covers the two main activities of the Zurich group at CERN on the ATHENA and CMS experiments between 1 April 2004 and 31 March 2005. It does not include the activity of one of us (C.A.) within the Particle Data Group, contributing to the "Review of Particle Physics" and the "Particle Physics Booklet". Further details on the group activities and publication reprints can be obtained from our home page (http://www.cern.ch/unizh/).

1 Production and Spectroscopy of Antihydrogen

C. Amsler, I. Johnson, N. Madsen‡, H. Pruys, C. Regenfus, and J. Rochet

In collaboration with: CERN, University of Aarhus, Brescia, Genoa, Pavia, RIKEN,
Rio de Janeiro, Swansea, Tokyo (ATHENA Collaboration).
‡ Now at the University of Aaarhus, Denmark

1.1 Introduction

Following the first observation of cold antihydrogen ($\bar{H}$) in 2002 [1], the ATHENA collaboration continued to optimize the antihydrogen formation rate and to study the $\bar{H}$ production mechanisms when low energy antiprotons are merged with dense and cold positron plasma [2, 3, 4, 5]. In this report we summarize the results achieved in 2004. The Zurich group has developed a new technique to measure the Lorentz deflection angle in silicon microstrip detectors [6]. We have also performed a feasibility study to measure the gravitational acceleration of antimatter. Two unforeseen obstacles have been encountered by ATHENA for spectroscopy experiments with cold $\bar{H}$: first, antihydrogen appears to be formed before thermalization in the nested Penning trap that we are using. The kinetic energy is then too high to confine the $\bar{H}$ atoms in the inhomogeneous magnetic field of e.g. a quadrupole or mutipole trap. Second, the $\bar{H}$ production mechanism (radiative or three-body combination) is still ambiguous. If three-body combination dominates ($e^+e^+\bar{p} \rightarrow \bar{H}e^+$) then 1s - 2s spectroscopy is not straightforward, since this mechanism populates the high Rydberg states of the $\bar{H}$ atom. Ways are in sight to solve these issues, but this will require significant time and R & D efforts.

The ATHENA positron-antiproton mixing trap comprises a series of hollow cylinders at 15 K generating the axial (z) potential configuration of a nested Penning trap. The radial confinement is provided by a 3 T axial magnetic field. The detector for $\bar{p}$ and e^+ annihilation built by the Zurich group [7] surrounds the mixing trap. It consists of two cylindrical layers of double-sided silicon strip detectors (radii of 4 cm and 5 cm) to register the charged annihilation pions and to reconstruct the annihilation vertex. Each layer contains 16 double-sided modules with active lengths of 16 cm. Antihydrogen is detected by requiring the spatial and temporal coincidence of the vertex with two back-to-back 511 keV γ's produced by the annihilation of the positron. The γ's are detected by a high granularity electromagnetic detector comprising 192 CsI crystals with avalanche photodiode readout. A detailed description of the ATHENA apparatus can be found in ref. [8].

1.2 Measurement of the Lorentz angle

We have measured the Lorentz deflection angle in microstrip sensors operated at a temperature of 130 K in a 3 T magnetic field. This measurement was performed with cosmic ray data and the ATHENA microstrip detector. The detector axis was parallel to the homogeneous 3 T solenoidal magnetic field. Thus the charge drift is perpendicular to the magnetic field.

Due to the propagation of charge carriers along the Lorentz angle, the charge spread at the collection surface is distorted in length and displaced. Impact positions for charged particles are reconstructed with a center of gravity algorithm of charge collected by adjacent strips. Tracks that traverse the silicon parallel to the Lorentz deflection generate the shortest charge spread and have similar charge collection properties to tracks that cross perpendicular to the sensor plane in the absence of magnetic field. A geometric model that relates the track inclination to the average cluster width has been developed to measure the Lorentz angle [6].

Cosmic rays traversing both cylinders were reconstructed from the four 3D points by requiring charged particles to fully traverse both cylinders. The four spatial measurements were fitted with a helix for data with the magnetic field on, and a straight line for data without magnetic field. The

Lorentz angle was measured by fitting the model to distributions of the average cluster size as a function of track inclination. The data sample was divided into ϕ and θ intervals (polar and azimuthal angle). Three distributions are shown in fig. 1.1. As expected, the data taken without magnetic field are symmetric around $\theta = 0$ (perpendicular incidence), while data taken with magnetic field are shifted towards positive values. The data are in excellent agreement with the model fits. These measurements correspond to holes drifting in sensors operated at 130 K in a 3 T magnetic field, and with an average internal electric field of 1.3 kV/cm. The Lorentz angle was found to be 19.6 $^{+1.0}_{-0.6}$ degrees [6].

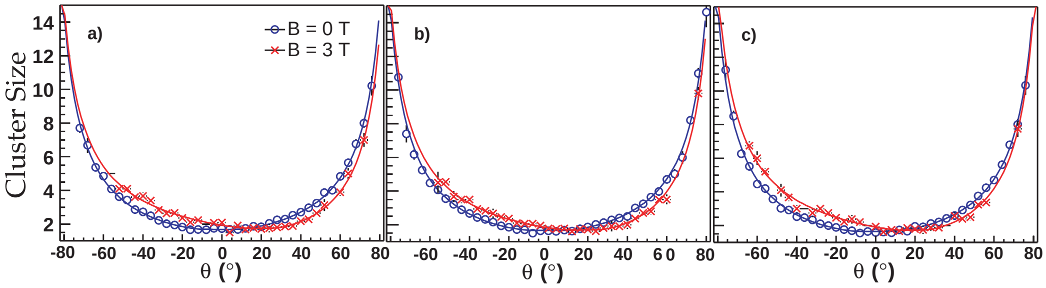

Figure 1.1: *Distribution of the average number of strips vs. inclination angle θ in three intervals of ϕ; around ϕ = -20°(a), 0° (b) and 20° (c) for field–off (circles) and field–on (crosses). The curves show the model fits.*

1.3 $\bar{H}$ production mechanism

Antihydrogen production is carried out by first loading the mixing trap with 7×10^7 e^+ which cool to the ambient temperature of 15 K by the emission of synchrotron radiation, and then by injecting about 10^4 $\bar{p}$ that interact through the Coulomb interaction with the e^+ plasma. We let the antiprotons interact with the positrons for about 180 s before ejecting both species and restarting the cycle. Neutral $\bar{H}$ atoms drift towards the electrodes of the mixing trap where they annihilate.

The two relevant mechanisms for $\bar{H}$ formation are two-body radiative recombination (in which a photon removes the binding energy) and three-body combination (in which a second positron removes the excess energy). The two processes lead to different n-state populations, the former populating mainly the low n states (this is the relevant process for the 1s - 2s laser spectroscopy) and the latter mainly the high n states. The two processes have also different temperature dependences, $T^{-1/2}$ for the former and $T^{-9/2}$ for the latter. We have measured the temperature dependence of $\bar{H}$ formation [3] by changing the positron plasma temperature with a radio-frequency excitation. Neither of the two power laws gives a good fit to the data, although the $T^{-1/2}$ dependence provides a better description. Since $\bar{H}$ is still produced at room temperature, radiative combination is favored over three-body combination.

However, the observed high antihydrogen production rate (peak rate of 440 ± 40 Hz [2]) is incompatible with the much smaller rate ($<$ 40 Hz) predicted by the two-body radiative process. In fact, some recent Monte Carlo calculations based on the three-body process [9] are consistent with the oberved high rate of antihydrogen production and the fraction of atoms ($\sim$ 15 %) that are sufficiently bound to escape the potential well and annihilate on the trap wall where they are detected.

Hence the cooling dynamics of the antiprotons in the mixing trap remains ambiguous and calls for more sophisticated measurements and calculations. To obtain further information on the recombination mechanism an attempt was made to stimulate radiative combination. We used a CO_2 laser to stimulate the two-body process from the continuum to the n = 11 antihydrogen bound state. The laser system in shown in fig. 1.2. The laser beam was focused at the center of the positron cloud (beam waist 2σ = 2.0 mm). The wavelength of the laser was tuned by changing the angle of the grating

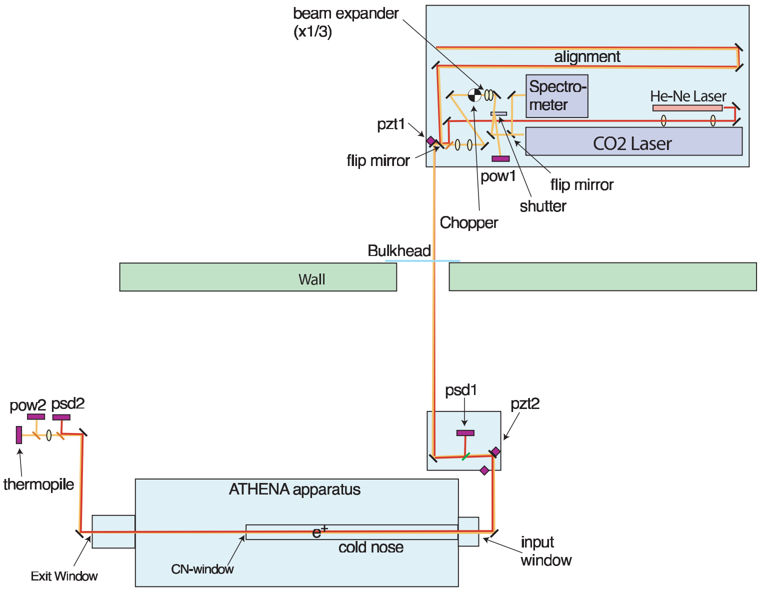

Figure 1.2: *Laser setup used in 2004 to stimulate the formation of antihydrogen.*

which also served as the high reflecting mirror at one end of the laser cavity. The wavelength could be tuned from 9.5 μm to 11.2 μm. At the optimum wavelength of 10.96 μm the rate of stimulated two-body radiative combination was expected to be 60 Hz, a rate enhancement easily detectable by the Zurich detector. The laser power was 100 W $\cdot$ cm^{-2} and the transmission to the mixing trap 70 %, measured by a laser power meter at the end of the ATHENA main magnet, and directly at the exit of the laser.

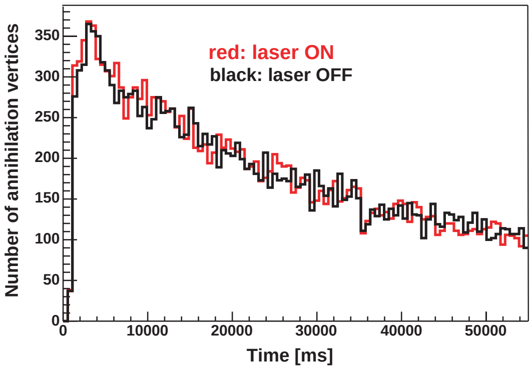

Figure 1.3: *Annihilation rate as a function of time for laser ON and laser OFF.*

Figure 1.3 shows the time distribution of annihilation vertices with and without laser stimulation. There is no obvious enhancement, although the data still need to be analyzed in detail. The absence of stimulation favours the three-body recombination mechanism.

1.4 $\bar{H}$ angular distribution

We have shown that about 65 % of all observed annihilations were due to antihydrogen [2]. Hence the detection of the two 511 keV γ's that led to the unambiguous observation of antihydrogen in ref. [1] (golden events) but which was inefficient ($\sim 2.5 \times 10^{-3}$) is not really required to study the production mechanism. Hence the spatial distribution of the emerging $\bar{H}$ atoms was studied without

γ-coincidence to increase the size of the statistical sample [5]. Figure 1.4 shows the vertex distribution along the z axis for all annihilations (a) and for $\bar{p}$ annihilations without e^+ mixing (b). Subtracting (b) from (a) (and applying a cut for the so-called hot spots in the transverse projection [10]) leads to the z distribution of annihilating $\bar{H}$ atoms (fig. 1.4c). The distribution is in good agreement with the one obtained with the 2γ-coincidence.

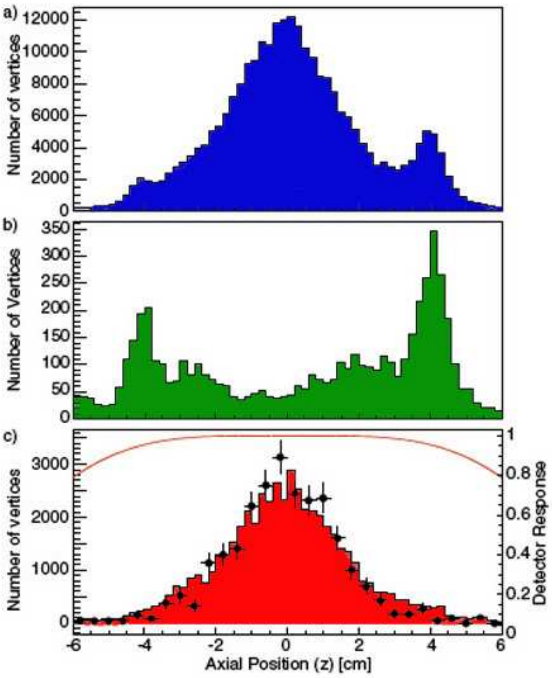

Figure 1.4: *Distribution of annihilations along the trap axis (z) (a) for all vertices during cold mixing (1.75 $\times$ 10^5 events) and (b) for $\bar{p}$ annihilating in a nested trap without e^+ (5717 events). The colored area in (c) shows the difference after eliminating hot spots (4.9 $\times$ 10^4 events). The full circles show $\bar{H}$ annihilations when two back-to-back 511 keV photons are required in coincidence. The solid line gives the detector acceptance.*

Figure 1.5 shows that $\bar{H}$ atoms tend to move preferably along the z axis, although the distribution is not far from isotropy. The distribution is independent of the positron temperature (but the formation rates decreases with positron temperature). A model has been developed assuming a positron plasma rotating at a frequency of 80 kHz. The plasma was typically 2.5 mm in radius, 32 mm in length, and had a density of 1.7 $\times$ 10^8 cm^{-3}. The data in fig. 1.5 are consistent with a two-temperature Maxwellian model for the velocities of the produced antihydrogen. In the axial direction the kinetic energy is typically an order of magnitude larger than in the transverse direction. The formation temperature is 150 K in the axial direction if the equilibrium temperature (15 K) is reached in the transverse direction. Hence antihydrogen is *not* produced at thermal equilibrium between the two plasma.

These are bad news for trapping antihydrogen and for performing $\bar{H}$ spectroscopy since typical neutral traps have depths of about 1 K. Therefore very few $\bar{H}$ will be trapped. To produce cold $\bar{H}$ it is thus necessary to have cold antiprotons before mixing with positrons.

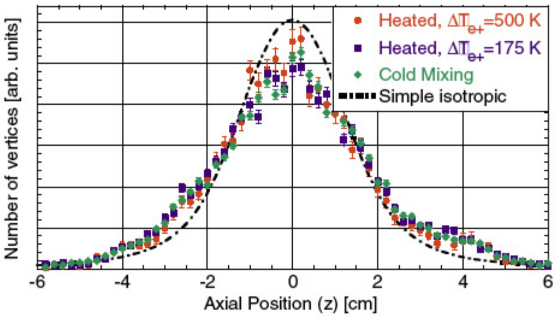

Figure 1.5: *Distribution of antihydrogen annihilation along the trap axis (z) for cold mixing and mixing with positrons heated to two different temperatures. The dot-dashed line is the prediction for isotropic emission from the positron plasma volume. The distributions have been normalized to the same area.*

1.5 Outlook

A possible solution to confine $\bar{H}$ could be to invert the current mechanism for formation and trap the antiprotons in the center of the nested trap, cooling them first with electrons. This means that the $e^+\bar{p} \to \bar{H}$ mechanism needs to be studied in a completely new configuration. The presence of the magnetic field gradient needed for the neutral trap also strongly influences the stability of the confinement of the charged particles. One of the major issues is the breaking of the rotational symmetry induced by the presence of the radial magnetic field having values comparable to the axial magnetic field of the charged particle trap.

The conceptual design that we are currently investigating foresees a mixing region that allows the confinement of positrons, antiprotons and the neutral antihydrogen atoms in the same volume. This is achieved by superimposing a trap for charged particle confinement with a trap for antihydrogen, made by a radial multipolar magnetic gradient together with an axial magnetic bottle. This issue is being pursued by our colleagues from Genoa with electrons and protons combining to form hydrogen. A Lyman-α laser with sufficient power for the laser cooling of antihydrogen atoms is being considered by collaborators from Florence.

1.5.1 Antimatter gravity

Assuming CPT symmetry antimatter $\bar{M}$ would fall on an anti-earth with the same acceleration g as matter M on the earth. However, CPT does not make any statement on the acceleration $\bar{g}$ of antimatter by the earth. In quantum field theories (QFT), forces mediated by the exchange of bosons with spin 1 may be repulsive or attractive (such as the γ of QED) while spin 0 and 2 exchanges are attractive. However, a QFT formulation of general relativity with a tensor T (the spin 2 graviton) is inconsistent. Extensions including supersymmetric partners of the graviton lead to vector V (spin 1) and scalar S (spin 0) exchanges. At least partial cancellation of V and S interactions is expected in MM while attractive coherence is predicted for $M\bar{M}$. Therefore antimatter will fall on earth with a larger acceleration than matter. The size of the effect depends on the relative strength between S and V exchanges. Measurements performed with Eötvös-type experiments on MM lead to predictions for the relative difference between g and $\bar{g}$ varying between 10 % and 2×10^{-6}.

We have investigated the feasibility of a pilot experiment with $\bar{H}$ atoms with energies of typically 1 K. For a 1 m flight distance the gravitational sag of a single, horizontally emitted, $\bar{H}$ atom of 1 K kinetic energy could be measured to within a few percent if the emission point, initial flight direction and energy of the atom are known. Better precisions can be reached with $\bar{H}$ atoms with energies below 1 K. A possible experiment coupled to an $\bar{H}$ source would consist of horizontal slits and a position sensitive $\bar{H}$ detector to measure the sag of the interference pattern. The best solution uses a Mach-Zehnder matter wave interferometer consisting of two identical transmission gratings (fig. 1.6, left). Such a device was used for measurements of g with cold atoms or neutrons [11]. It does not require a monochromatic atomic source since the interference pattern is independent of wavelength. However, the divergence of the beam must be sufficiently small to avoid smearing.

The sag can be determined with high precision by rotating the setup around the beam axis by 90° (slits vertical). The gravitational sag for a distance L = 1 m is shown in fig 1.6 (right) as a function of temperature. A temperature of 0.5 K (typical for a multipole trap) corresponds to a sag of 400 μm.

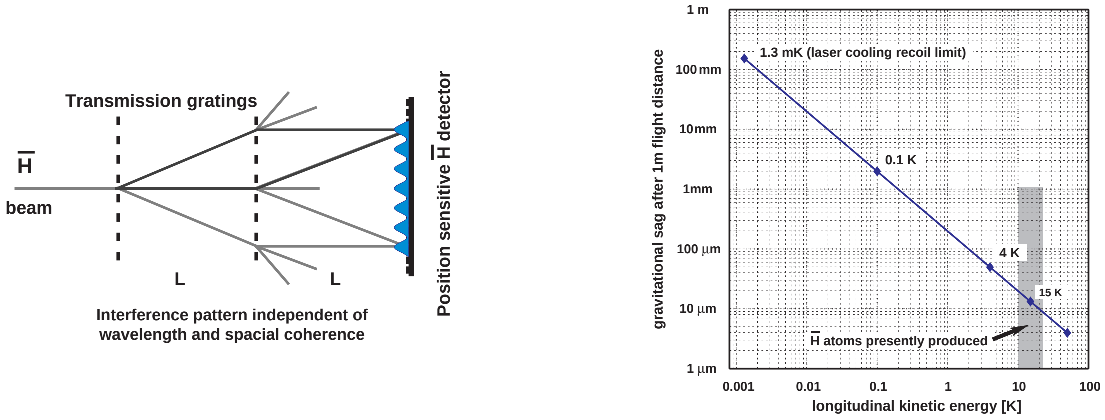

Figure 1.6: *Left: Mach-Zehnder interferometer with two identical transmission gratings and position sensitive $\bar{H}$ detector. Right: Gravitational sag of $\bar{H}$ atoms in the gravitational field after 1 m flight distance (assuming $\bar{g}$= 9.81 m/s^2).*

We assume that a spatial resolution of 5 μm for the annihilation point on the detector surface can be achieved and plan to use a silicon microstrip detector detecting the $\bar{H}$ annihilations with spatial *and* time-of-flight information. The extraction of the atoms from the neutral trap could be done by either lowering one of the axial magnetic wells or kicking the $\bar{H}$ out with a magnetic pulse. Since the time of flight is in the range of 100 ms, only a moderate resolution on the kick-out time is required.

A proposal to the CERN Committees will be submitted in due time, depending on the results of the R&D efforts mentioned above. The ATHENA project itself was completed in December 2004 with the closure of the antiproton decelerator for at least 18 months.

References

[1] M. Amoretti *et al.* (ATHENA Collaboration), Nature **419** (2002) 456
[2] M. Amoretti *et al.* (ATHENA Collaboration), Phys. Lett. **B 578** (2004) 23
[3] M. Amoretti *et al.* (ATHENA Collaboration), Phys. Lett. **B 583** (2004) 59
[4] M. Amoretti *et al.* (ATHENA Collaboration), Phys. Lett. **B 590** (2004) 133
[5] N. Madsen *et al.* (ATHENA Collaboration), Phys. Rev. Lett. **94** (2005) 033403
[6] I. Johnson *et al.*, Nucl. Instr. and Meth. in Phys. Res. **A 540** (2005) 113
[7] C. Regenfus, Nucl. Instr. and Meth. in Phys. Res. **A 501** (2003) 65
[8] M. Amoretti *et al.*, Nucl. Instr. and Meth. in Phys. Res. **A 518** (2004) 679
[9] F. Robicheaux, Phys. Rev. **A 70** (2004) 022510
[10] M. Fujiwara *et al.*, Phys. Rev. Lett. **92** (2004) 065005
[11] M. Gruber *et al.*, Phys. Lett. **A 140** (1989) 363;
D. W. Keith *et al.*, Phys. Rev. Lett. **66** (1991) 2693.

2 Particle Physics with CMS at the LHC

Y. Allkofer, C. Amsler, V. Chiochia, A. Dorokhov, C. Hörmann, K. Prokofiev, H. Pruys,
C. Regenfus, P. Robmann, J. Rochet, T. Speer, S. Steiner, and D. Tsirigkas‡

In collaboration with: ETH-Zürich, Paul Scherrer Institut (PSI) and the CMS Collaboration.
‡ CERN doctoral student

2.1 Physics programme

The Higgs boson mass is predicted to be smaller than 251 GeV (95 % C.L.) and LEP experiments have set a lower experimental limit of 114 GeV (95 % C.L.). A light Higgs decays mainly to $b\bar{b}$, a heavy Higgs mainly to four leptons via WW or Z^0Z^0 (fig. 2.1a). However, the two-gluon $gg \rightarrow b\bar{b}$ background dominates the signal for a light Higgs. For CMS one of the sensitive channels to search for a light Higgs is $H \rightarrow \gamma\gamma$ (fig. 2.1b) . This is the motivation for the large electromagnetic calorimeter made of 80'000 $PbWO_4$ crystals.

The LHC is scheduled to start operations in 2007 at a center of mass energy of $\sqrt{s}$ = 14 TeV. The target luminosity is 10^{34} $cm^{-2}s^{-1}$ which corresponds to an integrated luminosity of about 1 fb^{-1}, achieved every day, assuming full efficiency. This luminosity will hopefully be reached after 2 - 3 years of LHC operation. Figure fig. 2.1b shows the required integrated luminosity for a 5σ Higgs discovery, as a function of mass. Since the final luminosity will not be obtained immediately, the Higgs is not likely to be observed during the commissioning years, unless it is rather heavy (see fig. 2.1b).

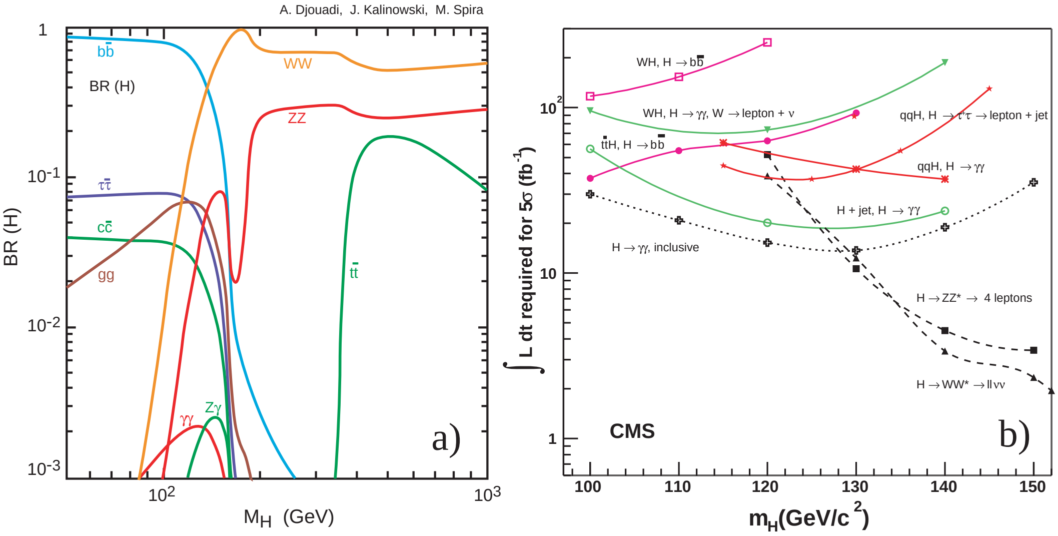

Figure 2.1: *a) Higgs decay branching ratios as a function of Higgs mass; b) Integrated luminosity required for a discovery with statistical significance of 5σ (1 fb^{-1} represents 1 day of LHC operation at full luminosity and efficiency).*

The Zurich group has therefore decided to concentrate first on issues related to B meson physics. At the LHC the cross section for $b\bar{b}$ production is five orders of magnitude higher than at the Tevatron and 10^4 $b\bar{b}$ pairs/s will be produced, even with a reduced luminosity of 10^{33} $cm^{-2}s^{-1}$. Also the physics involving B_s mesons ($\bar{d}s$ and $\bar{s}d$) will not be covered at the current B factories (since the $Y(4s)$ does not decay to $B_s\bar{B}_s$). For B physics the pixel detector we are constructing will be essential to tag secondary vertices from B decays.

We are preparing [1] a high statistics measurement of the decay channel $B_s \to J/\psi\ \phi$ with $J/\psi \to \mu^+\mu^-$ (or e^+e^-) and $\phi \to K^+K^-$. This channel is one of the golden channels to study many properties of B_s mesons such as CP violation in the B_s system and $B_s - \bar{B}_s$ oscillations. The search for rare B_s-decays such as $B_s \to \mu^+\mu^-$, $B_s \to \mu^+\mu^-\phi$, which have not been observed, opens windows for new physics beyond the standard model. Our experience with the reconstruction of B mesons at CMS will then be quite useful to search for the Higgs in a cleaner environment, such as the associated production $t\bar{t}H, H \to b\bar{b}$, leading to four jets containing b-quarks.

2.2 Performance tests of the silicon pixel detector

To reconstruct B mesons and suppress the dominating light quark and gluon background one has to determine the primary interaction and secondary B decay vertices. The optimum resolution is achieved with the first detector layer as close as possible to the beam-beam collision point. The first layer of our silicon pixel detector is at a distance of $\sim$ 4 cm from the interaction point. The very high particle flux near the primary vertex ($\sim$ 1000 particles every 25 ns) requires a highly granular detector composed of pixels delivering 3D coordinates with resolutions of the order of 15 μm.

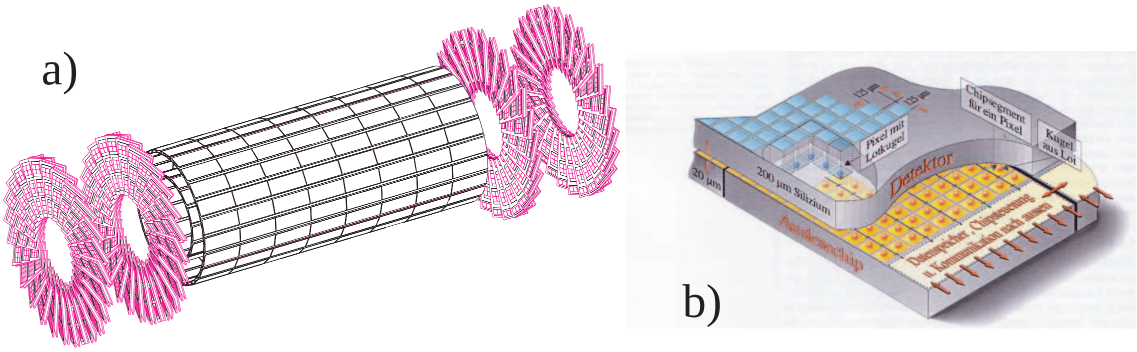

Figure 2.2: *a) the CMS pixel vertex detector; b) Schematic view of a pixel detector element. Each sensor pixel is connected through an indium solder bump to a pixel unit cell on the readout chip which amplifies and processes the signal. The data are stored at the periphery of the chip where they wait for trigger confirmation.*

The pixel detector consists of three concentric cylindrical layers, 53 cm long, with radii of 4.4, 7.3 and 10.2 cm and forward/backward wheels (fig. 2.2a). The latter wheels will be provided by the US collaborators while the barrel layers are built by the Swiss groups. The pixels are mounted on segmented sensor plates with readout chips in 0.25 μm technology, connected by indium bump bonds (fig. 2.2b). The analogue signals are read out to determine the coordinates more accurately, using charge sharing between pixels.

Radiation hardness is the main concern. We are using oxygen enriched silicon substrates which are more resistant to radiation. The pixels are formed by isolated n^+ implants and the pn junction is formed by a large p^+ implant on the backside (fig. 2.3). The thickness of the sensor is 285 μm and the pixel size is 100 $\times$150 $\mu\mathrm{m}^2$. The pixels must be separated by p^+ type isolation in order to prevent conductive interconnection between them caused by electron accumulation close to the surface between pixels. Two designs of p^+ dopants separations were tested, the p-spray design (fig. 2.3, left) for which a moderate boron spray concentration has been diffused between pixels (produced by CiS, Erfurt), and the p–stop ring structure (fig. 2.3, right) with very high boron concentration surrounding every pixel (manufactured by SINTEF, Oslo). To keep the pixel potential close to the readout chip potential (in the event of a pixel loosing the indium bump connection) the pixels are not completely isolated from each other. The high resistive inter–pixels connection is achieved by a

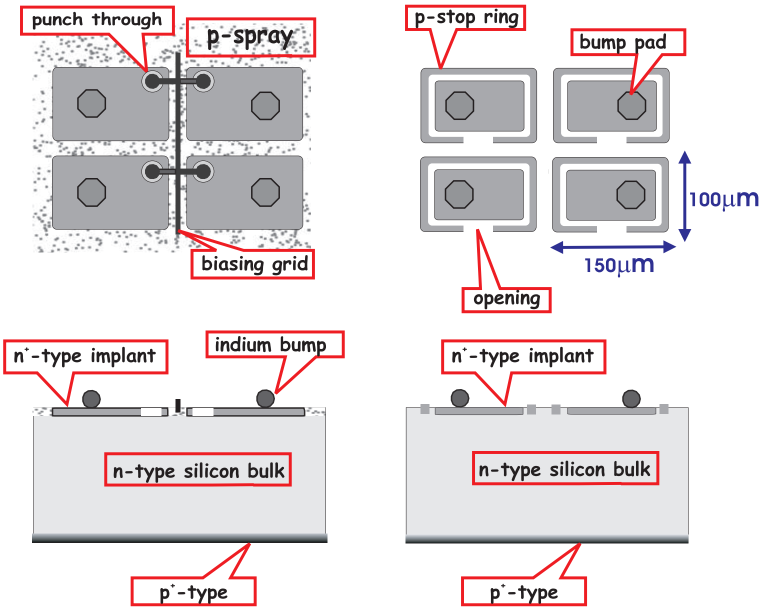

Figure 2.3: *Front view and cross section of the p-spray (left) and p-stop designs (right).*

punch–through structure and biasing grid in the the p–spray design and a gap in the p–rings for the p–stop design.

In 2004 we tested the performances of various pixel designs before and after irradiation. The pixel dimensions were of the former design (125 $\times$ 125 μm^2). They were irradiated up to a fluence of 10^{15} n$_{eq}$/cm^2 (neutron equivalent dose per unit surface) with 24 GeV protons from the CERN PS. For comparison the first four years of LHC operation gradually converging to the nominal luminosity correspond to 6 $\times$ 10^{14} n$_{eq}$/cm^2 for the innermost (4.4 cm) pixel layer.

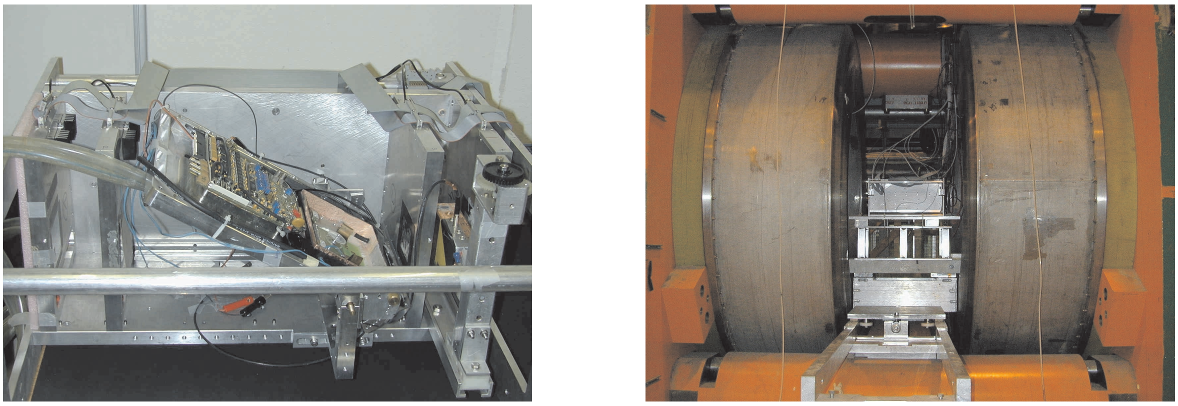

Figure 2.4: *Left: Pixel sensor prototypes and readout inserted beween the third and fourth plane of the silicon beam telescope. Right: Helmholtz coils providing a magnetic field of 3T.*

The samples were tested with 150-225 GeV pions in the H2 beam line of the CERN SPS in 2003 and 2004 [2, 3]. The beam test setup consisted of our beam telescope [4] made of 8 silicon microstrip detectors (4 measuring the horizontal x and 4 the vertical y impact points) with 50 μm readout pitch and a fast trigger diode. The pixel sensors were bump-bonded to an earlier readout chip (PSI30) and were mounted on a rotating support positioned between the second and third plane of the beam telescope (fig. 2.4, left). The samples were stabilized at a temperature of -10 °C by means of water cooled Peltier elements. The hit coordinates on the sensor could be determined from the telescope with a resolution of $\sigma \sim 1$ μm. The telescope was inserted in the gap between two superconducting Helmholtz coils providing a field of 3 T (fig. 2.4, right). Measurements were performed with the field parallel to the beam (to measure the Lorentz angle, see below) and perpendicular to the beam (to measure the position resolution).

With our high resolution telescope it was possible to scan the surface of the sensors and to determine the charge collection efficiency. Irradiated sensors show trapping of charge carriers and the bias voltage has to be increased from typically 100 to 450 V to collect more charge and reach full depletion. Figure 2.5 shows the average charge collected for p-spray and p-stop before and after irradiation. The region with the highest collection efficiency is in the central part of the pixel corresponding to the n^+ implants. The charge collection efficiency is higher than for the p-stop design, about 60 % of that for unirradiated sensors after a fluence of 10^{15} n_{eq}/cm^2. The charge collection efficiency is lower in the punch-through regions in the case of the p-spray design. The p-spray and p-stop designs which were exposed to a fluence of 6×10^{14} n_{eq}/cm^2 have a particle detection efficiency of 99 % with a threshold of 2000 electrons. The respective value for the p-stop design is somewhat lower, 95 %. The p-spray design is therefore preferred over the p-stop.

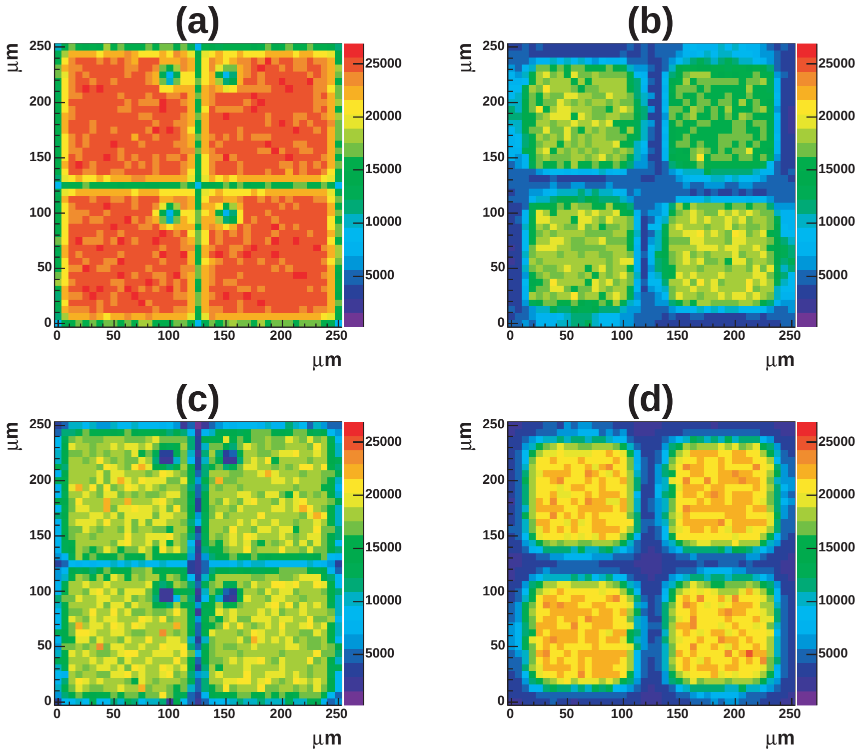

Figure 2.5: *Collected charge over the pixel surface at full depletion. Red (blue) correponds to high (low) charge levels. The number of collected electrons is shown in the righthand bars. The plots on the left show the p-spray types before (a) and after irradiation with 6.7 $\times$ 10^{14} n_{eq}/cm^2 (b). The plots on the right show the corresponding charge for the p–stop designs.*

The signal-to-noise ratio is about 70 for the unirradiated p-spray sensors, about 50 for the sensors exposed to a fluence of 6×10^{14} n_{eq}/cm^2, and about 10 for a fluence of 2.6×10^{15} n_{eq}/cm^2 (fig. 2.6). Based on the results of these measurements [3] we have chosen the p–spray design for the barrel sensors. The results from the 2004 tests show that the pixel sensors can be operated up to irradiation fluences of 10^{15} n_{eq}/cm^2. This is much higher than what was originally specified for the CMS pixel detector.

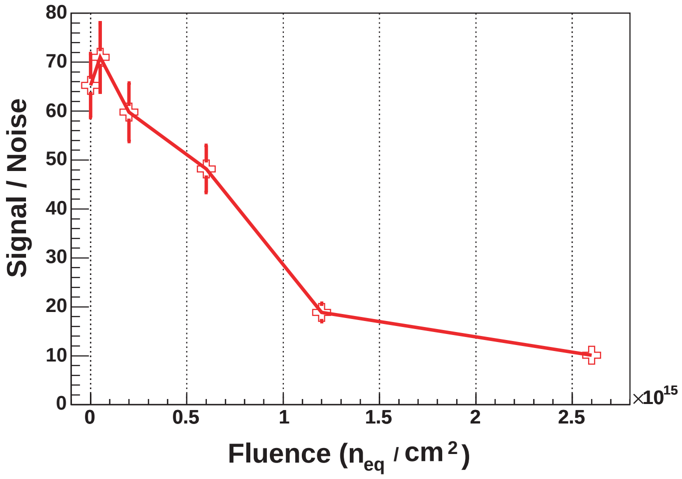

Figure 2.6: *Signal-to-noise ratio measured with the p-spray sensors as a function of irradiation.*

2.3 Charge collection as a function of depth

The charge collection depends on the location of the charge deposit in the sensor bulk. The electron–hole pairs created in the bulk of a fully depleted unirradiated sensor reach the electrodes and contribute to the signal, while for irradiated sensors the trapping centers reduce the probability that charge reaches the electrode. This results in a smaller signal. The charge collection efficiency was measured with high energy pions crossing the sensor at a grazing angle $\alpha = 15°$ with respect to the pixel surface. The pixels at the distance x from the impact point along the beam direction sense the charge deposit at a depth $d = x \tan\alpha$ in the sensor.

Figure 2.7a shows the average signal as a function of x for various bias voltages and for a fluence of 6×10^{14} n_{eq}/cm^2. The depletion is believed to start from the implant side after irradiation leading to type inversion. Thus charge should be collected only from the depletion region close to the pixel implant at low bias voltages. However, the measured dependence of the charge collection efficiency (shoulder at high voltages) indicates that even at low bias voltages the charge is collected from both sides of the sensor. This means that for the irradiated sensors the depletion starts from both sides of the sensor bulk. In the conventional picture the total collected charge is proportional to $\sqrt{V_{bias}}$ up to full depletion voltage. The total charge collected is shown in fig. 2.7b as a function of $\sqrt{V_{bias}}$. These curves do not exhibit the expected $\sqrt{V_{bias}}$ dependence, due the behavior of the electric field which does not vary linearly across the sensor depth, as expected for unirradiated devices. This observation is supported by the direct measurement of the electric field in the sensor bulk [3] and by a detailed simulation [5].

2.4 Lorentz angle as a function of depth

In the presence of a magnetic field the electrons and holes, are deflected from their drift along the electric field lines. We have measured the deflection angle (Lorentz angle θ_L) as a function of depth in the 3 T field provided by the Helmholtz coils of fig. 2.4 (right), using the technique described in ref. [6, 7]. The beam enters the sensor plane at the grazing angle α and the magnetic field is parallel to the beam. Without magnetic field the charge generated at a given depth d would reach the pixel at a distance x along the beam line, as described in previous section. With magnetic field the charge is now deflected towards the adjacent pixel rows. Therefore, a measurement of the charge distribution among adjacent pixels yields the Lorentz angle θ_L as a function of x, and hence sensor depth [8].

Figure 2.8a shows the typical displacement of the collected charge at the surface of the sensor and

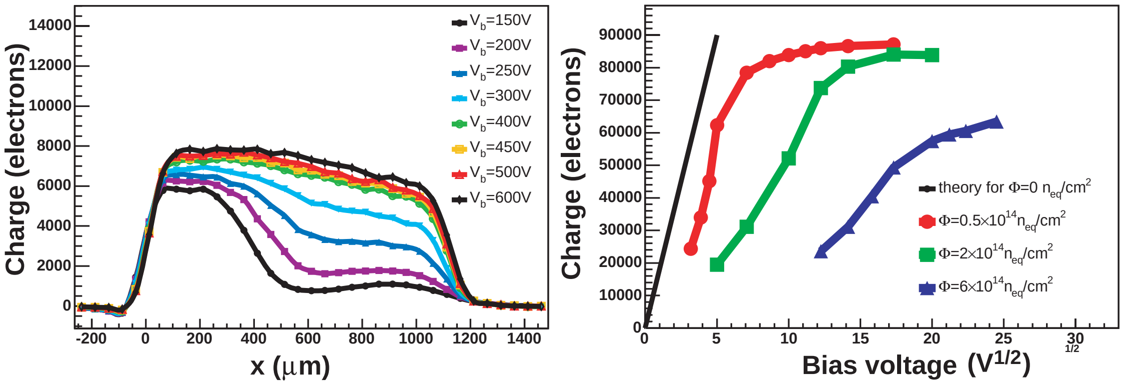

Figure 2.7: *(a) Signal as a function of x for sensors exposed to a fluence of 6* $\times$ 10^{14} *n_{eq}/cm^2 for various bias voltages; (b) Total collected charge as a function of the square root of the bias voltage far various fluences.*

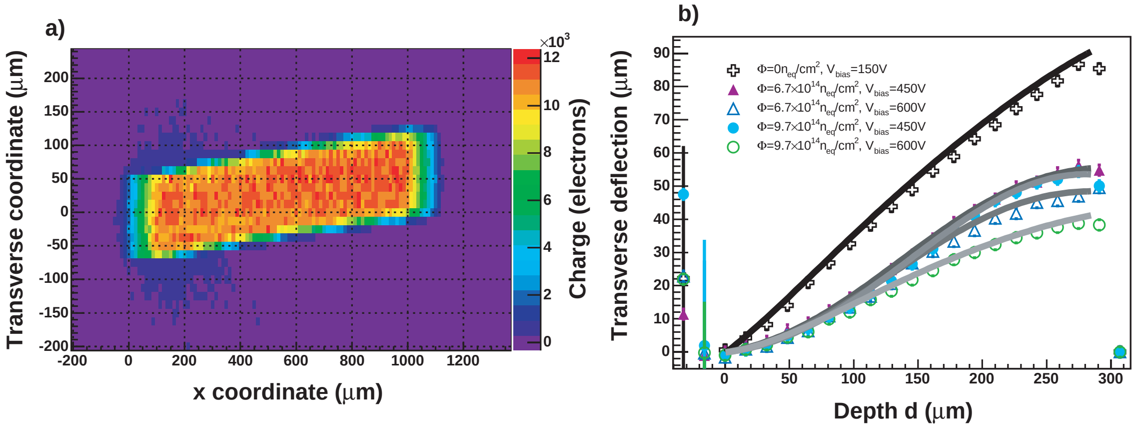

Figure 2.8: *(a) Deflection of the charge in a 3 T magnetic field. The beam enters the sensors from the left ; (b) Deflection at the surface as a function of the depth at which the charge was produced, for various fluences.*

fig. 2.8b the displacement of the charge as a function of the depth at which the charge was produced, for various irradiation levels. One observes that the the displacement (and hence θ_L) decreases with irradiation. This is simply due to the increasing electric field needed to fully deplete the sensor. Extrapolating to 4 T one finds a Lorentz angle of (26.3 ± 0.8)° close to the pixel implants for the unirradiated sensor (100 V bias) and (11.6 ± 1.4)° after 6.7 × 10^{14} n_{eq}/cm^2 (450 V bias).

Figure 2.9a shows how θ_L depends on the sensor depth for various irradiation levels. The Lorentz angle appears to depend on depth. Since θ_L depends on E, B and the mobility (the latter also being a function of E), a measurement of θ_L as a function of depth determines the behaviour of the electric field as a function of depth. Using a well known empirical parametrization of the mobility one can extract the electric field as a function of sensor depth [3]. Figure 2.9b shows that the electric field reaches maxima below both surfaces and a minimum in the bulk center.

2.5 Position resolution

The magnetic field was switched perpendicularly to the beam to reproduce the geometry of the CMS barrel sensors and the position resolution of irradiated sensors was measured with high energy pions

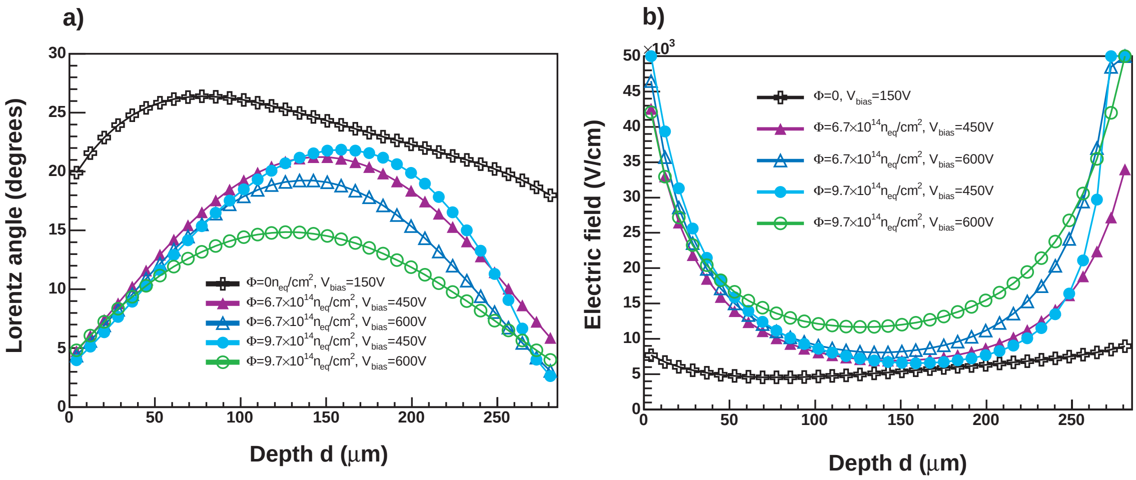

Figure 2.9: *(a) Lorentz angle θ_L as a function of depth; (b) Electric field as a function of depth. The regions immediately below the surfaces ($\sim$ 20μm) are affected by large systematic uncertainties.*

in a magnetic field of 3 T [3]. A simulation of the response of the 125 $\times$ 125 μm^2 was then performed, including the behaviour of the E-field described in the previous section, and verified with data. The simulation was then used to predict the expected charge sharing and the resolution for irradiated 100 $\times$ 150 μm^2 sensors of CMS at 4 T. Due to the widths of the (flat) modules the r.m.s resolution along the $r\phi$ direction (azimuthal angle direction) will vary with ϕ. It lies between 10 μm and 20 μm, depending on irradiation fluence and polar angle (fig. 2.10). After the first four years of operation the resolution at the innermost barrel layer is still below 20 μm along the $r\phi$ direction and depends weakly on the polar angle. The resolution along the z direction is better than 20 μm.

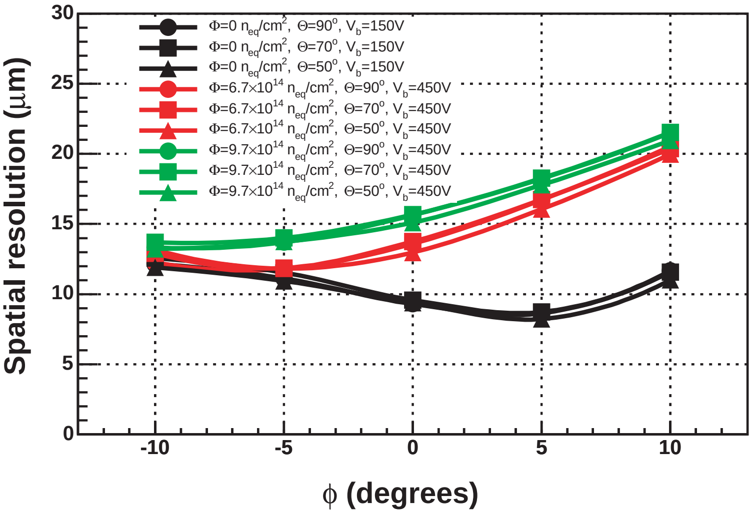

Figure 2.10: *Predicted $r\phi$ position resolution in the CMS pixel barrel as a function of azimuthal angle ϕ, for various polar angles θ and irradiation fluences.*

In conclusion, the pixel sensors for CMS will perform according to expectation and those at 4 cm from the collision point will fulfill the requirements at least during the first four years of LHC operation.

2.6 Mechanical support structure

The design and construction of the mechanical support structure for the CMS pixel detector is performed by our group and our Institute's workshop. The detector support structures (fig. 2.11, left) are made of aluminum tubes (wall thickness 300 μm) which are of trapezoidal shape to fit the geometrical constraints. The custom made 240 μm thick carbon fibre blades which support the pixel modules are then glued to the tubes forming the detector segments. Four to five of the aluminium tubes are laser-welded to an aluminum container which distributes the cooling fluid. Laser-welding is done in collaboration with industry. The manifold cools the detector modules to -20 °C using C_6F_{14} as a coolant. On both ends the manifolds are embedded in a carbon fibre support frame which supports the single segments and makes up the detector layer half shell.

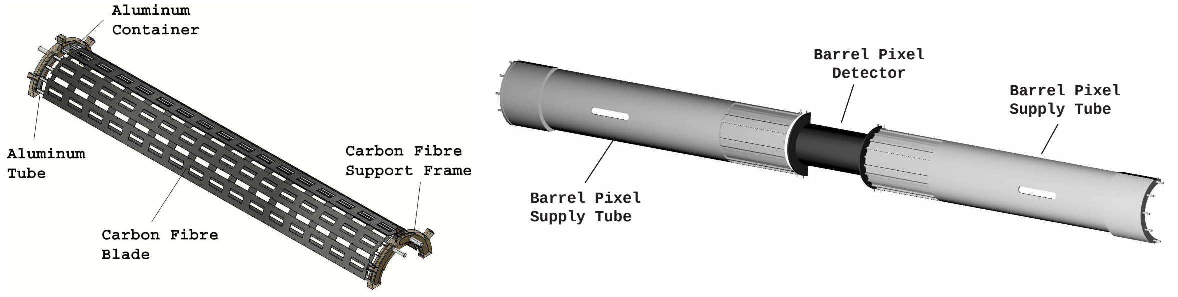

Figure 2.11: *Left: Design view of a half shell of the support structure for the innermost pixel layer. Right: Half shell of the barrel pixel detector system with its two service tubes.*

We are also building the two 2.2 m long service tubes (fig. 2.11, right) which transfer the power, all optical and electrical signals, and the cooling fluid to and from the detector. The power and slow control leads are embedded in the supply tube body. Foam will guarantee rigidity. The full system (pixel detector + service tube) is 5 m long. Two vertically separated half shells will be inserted into the CMS detector on a rail system. The insertion will be rather delicate since it will be done after the installation of the LHC beam pipe.

The design of the detector structure has been completed in 2004. The tools for the production of the different segment parts are also designed and manufactured. In 2005 we will continue with the leakage and cooling tests using the prototype segment of the support structure. Manufacturing of the final pixel segments and half shells will then start. Installation into CMS is foreseen during winter 2007/8, six months after LHC commissioning to avoid radiation damage during the initial injection trials.

2.7 Pixel power distribution

Our group is also responsible for the design of the CMS pixel detector power distribution for the front end electronics (low voltage) and the pixel sensors (high voltage) and cabling. The power lines are integrated in the service tubes discussed in the section above on mechanics.

In 2004 we have constructed a laboratory setup to mimic the behaviour of a section of the CMS pixel detector with respect to beam and settings induced voltage spikes. The system had to cope with sudden (100 ns) current excursions of 2 A in 50 m long power lines. Various solutions were tested to reduce the inductance of the cables. The setup includes a prototype power supply unit housed in a VME-like crate, a mainframe unit controlling up to six crates, various power cables of the foreseen lengths, a prototype section of the service tube and active loads which reproduce the power consumption of the CMS pixel modules.

The tests were performed to optimize the power supply units and the cable specifications to the pixel detector needs, i.e. to determine the need for additional electronics and grounding schemes. The development of the power supply unit is done in collaboration with CAEN, Viareggio, and preliminary results are encouraging.

2.8 Event reconstruction software

The Zurich group has adapted and implemented in the reconstruction software of CMS (ORCA) the Kalman filter (KF). This is a χ^2-square minimization which hence assumes that the track measuring errors are Gaussian distributed. Tracks are normally taken to be straight in the vertex neighborhood. We have improved on the KF by using more realistic helicoidal tracks in the homogeneous field of CMS. However, non-Gaussian noise (e.g. due to δ-electrons) is unavoidable. The distributions of the vertex pulls (difference between simulated and reconstructed values, divided by the measurement error) have a Gaussian core with tails.

We have shown that non-Gaussian noise can be taken into account with a Gaussian-Sum Filter (GSF) [9]. Here the distributions of the measurement errors and the estimated quantities are modelled by linear superpositions (components) of Gaussian distributions. The main component describes the core of the distribution and the tails are described by one or several additional Gaussians. Several solutions for the vertex are then calculated with all combinations of components. The final vertex is calculated as the weighted average of all solutions. The algorithm was tested with a simplified simulation in which the tracks parameters were smeared with a mixture of two Gaussians. The hit positions, error estimates and χ^2 are significantly improved.

The sensitivity of the GSF with respect to badly measured tracks or tracks assigned to the wrong vertex (outliers) was extensively studied. These tests demonstrate a higher degree of robustness than χ^2-square estimators and show the adaptive power of the GSF for outliers for which higher weights are assigned to track-components with the largest standard deviations. A novel idea which emerged from these tests was the combination of the GSF with another non-linear filter, the *Adaptive Vertex Filter* (AVF) [10, 11]. This filter is referred to as the *Adaptive-GSF* (A-GSF).

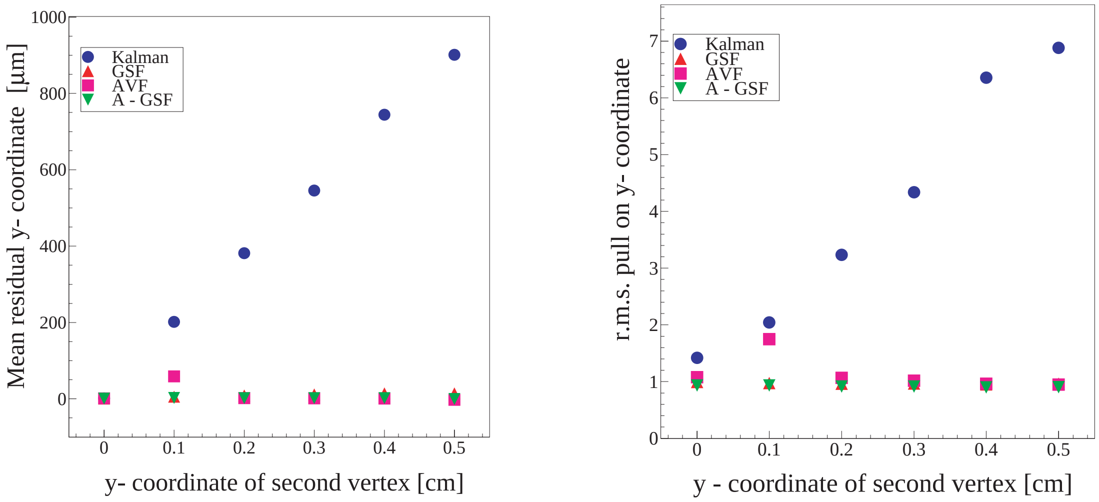

Figure 2.12: *Mean residuals (left) and standard deviations of the pull distributions (right) for different transverse positions of a vertex generated by an outlying track.*

For example, an outlying track originating from a second vertex is added to the four tracks from the main vertex. The position of this vertex is shifted by between 0 and 5 mm in the transverse y direction relative to the jet-axis from the main vertex. The values of the mean residual distribution and the pull of the estimated vertex are shown in fig. 2.12. The correct error assignments should lead to r.m.s. pulls of 1. The three non-linear filters are remarkably stable and improve substantially over the KF in terms of resolutions and pulls. For small displacements of the vertex, the AVF is not able to identify all of the outliers and is therefore slightly worse than the GSF and A-GSF. In particular situations the A-GSF performs much better than the GSF, but at the expense of a much longer CPU time.

In 2003/04 we also developed a kinematic fit based on Lagrange multipliers which incorporates additional constraints into the vertex fit to improve the resolutions. These constraints may be the masses of well known (long-lived) hadrons decaying to the observed particles, energy and/or momentum conservation, or collinearity in two-body processes. A further constraint of interest requires the momentum of the reconstructed B meson to be parallel to the vector pointing from the primary to the secondary vertex.

Considerable progress was made this year [1] . A framework for modelling the decay sequence is now provided. The fit allows for instance the reconstruction of complete decay chains, such as $B^- \rightarrow D^0 l^- \bar{\nu}_l$, followed by $D^0 \rightarrow K^- \pi^+$, $D^0 \rightarrow K^- \pi^+ \pi^0$ or $D^0 \rightarrow K^- \pi^+ \pi^- \pi^+$, where only the final long-lived particles are detected. The kinematic fit can also be performed with or without vertex constraint. The software is flexible enough so that new constraints can easily be included by the user.

One decay benefiting directly from such a kinematic fit is $B_s \rightarrow J/\psi\ \phi \rightarrow K^+ K^- \mu^+ \mu^-$, in which the Zurich group is particularly interested. This channel provides one of the best ways to determine the height η of the Unitarity Triangle. Here one measures the (CP violating) asymmetry between $B_s \rightarrow J/\psi\ \phi$ and $\bar{B}_s \rightarrow J/\psi\ \phi$. The CP-violating weak phase $\phi_{CKM} = [\arg(V_{cs}^* V_{cb}) - \arg(V_{ts}^* V_{tb})]$, measured in the rate asymmetry, is equal to $2\lambda^2 \eta \simeq 0.03$, where λ is the sine of the Cabibbo angle. A measurement of a significantly larger phase ϕ_{CKM} would indicate contributions from non-Standard Model processes. These parameters may be obtained by a classical maximum-likelihood analysis or by an angular correlation analysis.

Our group is involved in the analysis of this decay with simulated data to estimate the sensitivity of the CMS detector. We have devised a selection strategy that relies on the partial reconstruction of the four charged tracks, already at the stage of the high level trigger (HLT). Indeed, by restricting the track reconstruction to the first 5 hits (to save CPU time) the precision on the track parameters is already sufficient. At the first level the dimuon trigger selects two muons of opposite charges with a transverse momentum above 3 GeV/c, using only the measurements from the muon chambers.

In the HLT the muons stubs are projected into the tracker and all tracks in a cone around a muon candidate are reconstructed. We require the presence of two muons tracks of opposite charges with an invariant mass within 100 MeV of the mass of the J/ψ, as well as two kaon tracks of opposite charges with an invariant mass within 100 MeV of the ϕ mass. The four tracks are required to come from a common secondary vertex by imposing a requirement on the confidence level of the vertex fit. As CMS lacks particle identification (with the exception of muons) all charged tracks have to be considered as possible kaon candidates. This adds a significant contribution to the background from combinatorial ambiguities.

The kinematic fit is applied during offline reconstruction. The r.m.s. resolution in the invariant mass is 14 MeV and the corresponding resolution σ_{ct} on the mean decay path $c\tau$ = 438 μs in the B_s rest frame is 35 μm (fig. 2.13). A preliminary study shows that approximately 125'000 fully reconstructed B_s candidates will be obtained in the first year of LHC operation at the reduced luminosity of $2 \times 10^{33} \mathrm{cm}^{-2} \mathrm{s}^{-1}$.

We are also investigating the analogous decay $B_s \rightarrow J/\psi\ \phi$ where $J/\psi \rightarrow e^+ e^-$. This decay will increase the B_s sample but the reconstruction of low-momentum electrons is notoriously difficult. All these studies will be incorporated into the physics technical design report requested by CERN in summer 2005.

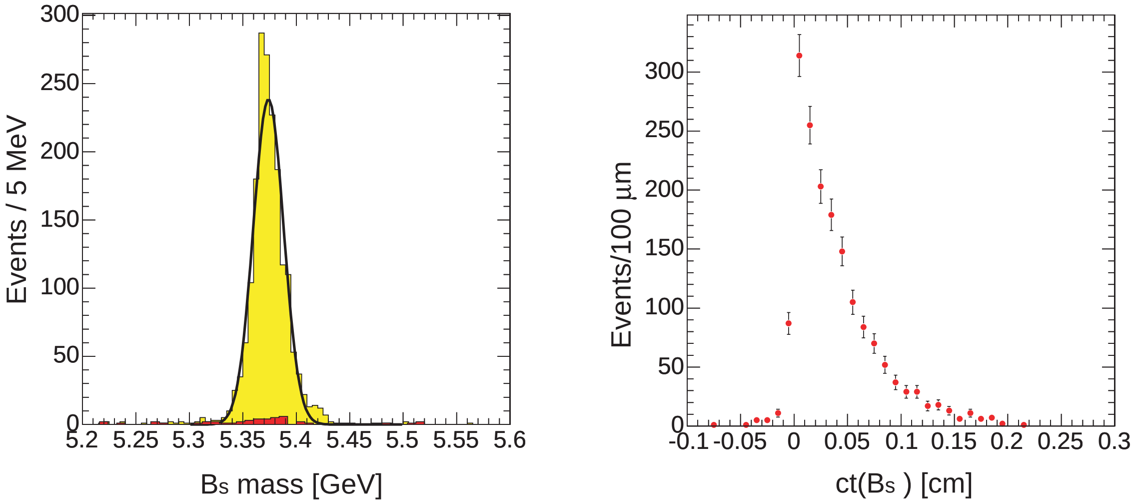

Figure 2.13: *Left: Invariant mass distribution of* $B_s \to J/\psi\ \phi$ *candidates after the kinematics fit. The small red area is the residual combinatorial background. Right:* ct *distribution.*

References

[1] K. Prokofiev, PhD thesis, in preparation

[2] A. Dorokhov *et al.*, Nucl. Instr. and Meth. in Phys. Research A **530** (2004) 71

[3] A. Dorokhov, PhD thesis, Universität Zürich, 2005

[4] C. Amsler *et al.*, Nucl. Instr. and Meth. in Phys. Research A **480** (2002) 501

[5] V. Chiochia *et al.*, Proc. 2004 IEEE Nuclear Science Symp., prep. physics/0411143

[6] R. Kaufmann, PhD thesis, Universität Zürich, 2001

[7] B. Henrich and R. Kaufmann, Nucl. Instr. and Meth. in Phys. Research A **477** (2002) 304

[8] A. Dorokhov *et al.*, Proc. Vertex 2004 Conf., prep. physics/0412036

[9] R. Frühwirth and T. Speer, Nucl. Instr. and Meth. in Phys. Research A **534** (2004) 217

[10] R. Frühwirth, K. Prokofiev, T. Speer, P. Vanlaer and W. Waltenberger, Nucl. Instr. Meth. in Phys. Research **A 502** (2003) 699

[11] J. D'Hondt, P. Vanlaer, R. Frühwirth and W. Waltenberger, IEEE Trans. Nucl. Sci. **51** (2004) 2037.

3 Publications

Articles

- Spatial Distribution of Cold Antihydrogen Formation
  N. Madsen et al. (ATHENA Collaboration)
  Phys. Rev. Lett. 94 (2005) 033403

- A measurement of the Lorentz angle in silicon strip sensors at cryogenic temperature
  I. Johnson, C. Amsler et al.
  Nucl. Instr. and Meth. in Phys. Res. A 540 (2005) 113

- Dynamics of antiproton cooling in a positron plasma during antihydrogen formation
  M. Amoretti, C. Amsler et al. (ATHENA Collaboration)
  Phys. Rev. Lett. B 590 (2004) 133

- Study of antiproton annihilation on neutrons into $\omega\pi^-\pi^0$
  C. Amsler et al. (Crystal Barrel Collaboration)
  Nucl. Phys. A740 (2004) 130

- Design and test of the CMS pixel readout chip
  M. Barbero et al.
  Nucl. Instr. and Meth. in Phys. Res. A 517 (2004) 349

- A Gaussian-sum filter for vertex reconstruction
  R. Frühwirth, T. Speer
  Nucl. Instr. and Meth. in Phys Res. A 534 (2004) 217

- Review of Particles Physics
  S. Eidelman et al. (Particles Data Group)
  Phys. Lett. B 592 (2004) 1

- Quark Model
  C. Amsler
  Phys. Lett. B 592 (2004) 154

- The $\eta(1405)$, $\eta(1475)$, f_1(1420), and f_1(1510)
  C. Amsler
  Phys. Lett. B 592 (2004) 549

- Non $q\bar{q}$ candidates
  C. Amsler
  Phys. Lett. B 592 (2004) 848

- Tests of silicon sensors for the CMS pixel detector
  A. Dhorokov, C. Amsler et al.
  Nucl. Instr. and Meth. in Phys. Res. A 530 (2004) 71

- Real-time detector for plasma diagnostic in antimatter experiment
  C. Carraro et al. (ATHENA Collaboration)
  Nucl. Instr. and Meth. in Phys Res. A 518 (2004) 249

- Production and detection of cold antihydrogen atoms
  M. Amoretti, C. Amsler et al. (ATHENA Collaboration)
  Nucl. Instr. and Meth. in Phys. Res. A 518 (2004) 244

- The first cold antihydrogen
  M. C. Fujiwara et al. (ATHENA Collaboration)
  Nucl. Instr. and Meth. in Phys. Res. A 532 (2004) 229
- Light exotic mesons
  C. Amsler
  Conf. on Quark Confinement and the Hadron Sprectrum, Gargnano, World Scientific (2003) 101
- Particle Physics Booklet
  S. Eidelman et al. (Particle Data Group)
  Extracted from Phys. Lett. B 592 (2004) 1
- Position Dependence of Charge Collection in Prototype Sensors for the CMS Pixel Detector
  T. Rohe et al.
  Proc. 2003 IEEE Nuclear Science Symposium
  physics/0312009, IEEE-TNS 51-3 (2004) 1150
- Performance of Radiation Hard Pixel Sensors for the CMS Experiment
  A. Dorokhov
  PhD Thesis, Universität Zürich, 2005

Articles in press

- Detection of antihydrogen with a silicon micro-strip and pure CsI detector
  I. Johnson et al. (ATHENA Collaboration)
  Proc. 8th ICATPP Conference
  physics/0401034, World Scientific (2004) 473
- ATHENA – First Production of Cold Antihydrogen and Beyond
  A. Kellerbauer et al. (ATHENA Collaboration)
  Proc. of the Third Meeting on CPT and Lorentz Symmetry, Bloomington
  hep-ex/040904, World Scientific
- Electric field measurement in heavily irradiated pixel sensors
  A. Dorokhov, Y. Allkofer et al.
  Proc. Vertex 2004 Conference
  physics/0412036, Nucl. Instr. and Meth. in Phys. Res. A
- Fluence dependence of charge collection in irradiated pixel sensors
  T. Rohe et al.
  Proc. 5th International Conference on Radiation Effects on Semiconductor Materials Detectors and Devices
  physics/0411214, Nucl. Instr. and Meth. in Phys. Res. A
- Simulation of Heavily Irradiated Silicon Pixel Sensors and Comparison with Test Beam Measurements
  V. Chiochia, et al.
  Proc. 2004 IEEE Nuclear Science Symposium
  physics/0411143, IEEE Transactions on Nuclear Science
- Final results on the neutrino magnetic moment from the MUNU experiment
  Z. Daraktchieva et al. (MUNU Collaboration)
  Phys. Lett. B

- Vertex reconstruction in CMS
  E. Chabanat et al.
  Nucl. Instr. and Meth. in Phys. Res.

- The effect of highly ionizing particles on the CMS silicon strip tracker
  W. Adam et al. (CMS Collaboration)
  Nucl. Instr. and Meth. in Phys. Res. A

- A Gaussian/sum filter for vertex reconstruction
  T. Speer
  Proc. of CHEP 2004, Interlaken

- A kinematic fit and a decay chain reconstruction library
  K. Prokofiev and T. Speer
  Proc. of CHEP 2004, Interlaken

Invited Lectures

- V. Chiochia
  Invited talk, IEEE Nuclear Science Symposium, Rome, 20.10.04
  ”Simulation of irradiated pixel sensors and comparison with test beam data”

- A. Dorokhov
  Invited talk, Vertex 2004 Conf., Menaggio, 16.09.04
  ”Pixel sensors under heavy irradiation”

- A.Dorokhov
  Seminar, Paul Scherrer Institut, 04.03.05
  ”Spatial resolution of the CMS pixel detector barrel module”

- I. Johnson
  Seminar, CMS tracker workshop, CERN, 19.01.05
  “Modeling and measuring the Lorentz deflection in silicon sensors”

- C. Regenfus
  Invited talk, Vertex 2004 Conf. , Menaggio, 15.09.04
  “The CMS pixel detector : a status report”

- T. Speer
  Invited talk, CMS workshop on b/tau Physics, Bari, 28.05.04
  “A kinematic fit library”

- T. Speer
  Invited talk, CHEP 2004 Conf., Interlaken, 30.09.04
  “A Gaussian-sum filter for Vertex reconstruction”

- T. Speer
  Invited talk, CHEP 2004 Conf., Interlaken, 30.09.04
  “Kinematic fit and decay chain reconstruction library”

ATHENA Collaboration (2004):
M. Amoretti, C. Amsler, G. Bonomi, A. Bouchta, P. Bowe, C. Carraro, C. L. Cesar, M. Charlton, M. Doser, V. Filippini, A. Fontana, M. C. Fujiwara, R. Funakoshi, P. Genova, J. S. Hangst, R. S. Hayano,

L. V. Joergensen, I. Johnson, V. Lagomarsino, R. Landua, E. Lodi Rizzini, M. Macri, N. Madsen, G. Manuzio, M. Marchesotti, P. Montagna, H. Pruys, C. Regenfus, P. Riedler, J. Rochet, A. Rotondi, G. Rouleau, G. Testera, A. Variola, D. P. van der Werf

MUNU Collaboration (2004):
Z. Daraktchieva, C. Amsler, M. Avenier, C. Broggini, J. Busto, C. Cerna, F. Juget, D.H. Koang, J. Lamblin, D. Lebrun, O. Link, G. Puglierin, A. Stutz, A. Tadsen, J.-L. Vuilleumier, V. Zacek

CRYSTAL BARREL Collaboration (2004):
C. Amsler, A.V. Anisovich, C. A. Baker, B. M. Barnett, C. J. Batty, M. Benayoun, P. Blüm, K. Braune, T. Case, V. Credé, K. M. Crowe, M. Doser, W. Dünnweber, D. Engelhardt, M. A. Faessler, R. P. Haddock, F. H. Heinsius, N. P. Hessey, P. Hidas, D. Jamnik, H. Kalinowsky, P. Kammel, J. Kisiel, E. Klempt, H. Koch, M. Kunze, U. Kurilla, R. Landua, H. Matthäy, C. A. Meyer, F. Meyer-Wildhagen, R. Ouared, K. Peters, B. Pick, M. Ratajczak, C. Regenfus, J. Reinnarth, A. Sarantsev, U. Strohbusch, M. Suffert, J. S. Suh, U. Thoma, I. Uman, S. Wallis-Plachner, D. Walther, U. Wiedner, K. Wittmack

PARTICLE DATA Group (2004):
S.Eidelman, K.G.Hayes, K.A.Olive, M.Aguilar-Benitez, C.Amsler, D.Asner, K.S.Babu, R.M.Barnett, J.Beringer, P.R.Burchat, C.D.Carone, C.Caso, G.Conforto, O.Dahl, G.D'Ambrosio, M.Doser, J.L.Feng, T.Gherghetta, L.Gibbons, M.Goodman, C.Grab, D.E.Groom, A.Gurtu, K.Hagiwara, J.J.Hernandez-Rey, K.Hikasa, K.Honscheid, H.Jawahery, C.Kolda, Y.Kwon, M.L. Mangano, A.V.Manohar, J.March-Russell, A.Masoni, R.Miquel, K.Monig, H.Murayama, K.Nakamura, S.Navas, L.Pape, C.Patrignani, A.Piepke, G.Raffelt, M.Roos, M.Tanabashi, J.Terning, N.A.Tornqvist, T.G.Trippe, P.Vogel, C.G.Wohl, R.L.Workman, W.-M.Yao, P.A.Zyla